



Autonomous rock classification using Bayesian image analysis for Rover-based planetary exploration

Helia Sharif^{a,*}, Maxim Ralchenko^b, Claire Samson^b, Alex Ellery^a

^a Department of Mechanical and Aerospace Engineering, Carleton University, Ottawa, ON, Canada K1S 5B6

^b Department of Earth Sciences, Carleton University, Ottawa, ON, Canada K1S 5B6



ARTICLE INFO

Article history:

Received 19 September 2014

Received in revised form

17 February 2015

Accepted 14 May 2015

Available online 7 July 2015

Keywords:

Autonomous geology

Textural analysis

Bayesian network

Haralick parameter

Planetary exploration

Exploration Rover

ABSTRACT

A robust classification system is proposed to support autonomous geological mapping of rocky outcrops using grayscale digital images acquired by a planetary exploration rover. The classifier uses 13 Haralick textural parameters to describe the surface of rock samples, automatically catalogues this information into a 5-bin data structure, computes Bayesian probabilities, and outputs an identification.

The system has been demonstrated using a library of 30 digital images of igneous, sedimentary and metamorphic rocks. The images are $3.5 \times 3.5 \text{ cm}^2$ in size and composed of 256×256 pixels with 256 grayscale levels. They are first converted to gray level co-occurrence matrices which quantify the number of times adjacent pixels of similar intensity are present. The Haralick parameters are computed from these matrices. When all 13 parameters are used, classification accuracy, defined using an empirical scoring system, is 65% due to a large number of false positives. When the number of parameters and the choice of parameter is optimized, classification accuracy increases to 80%. The best results were achieved with 3 parameters that can be interpreted visually (angular second moment, contrast, correlation) together with two statistical parameters (sum of squares variance and difference variance) and a parameter derived from information theory (information measure of correlation II).

The system has been kept simple not to draw excessive computational power from the rover. It could, however, be easily extended to handle additional parameters such as images acquired at different wavelengths.

© 2015 Elsevier Ltd. All rights reserved.

1. Introduction

Detailed mapping of a planet's surroundings from an exploration rover can reveal critical cues about the geology of the surface and past and present environmental conditions. Only nine rovers have successfully landed on other celestial bodies. Designed by the Soviets, Lunokhod 1 (1970) and 2 (1973) both traversed the lunar surface analyzing the mechanical properties of soil while transmitting close-up and panoramic images of their surroundings back to Earth. The Americans designed a Lunar Rover Vehicle (LRV) to assist the crew on their traverses on the surface of the moon during the Apollo 15 (1971), 16 (1972), and 17 (1972) missions. Moreover, four US-lead exploration rovers – Sojourner (1997), Spirit (2003), Opportunity (2003), and Curiosity (2012) – have identified a variety of geomorphological structures and geological materials on the surface of Mars. The ever-growing list includes alluvial fans with dominantly gravel-size sediment (Moore and Howard, 2005), meteorites (Schröder et al.,

2008), basalts with columnar jointing (Milazzo et al., 2009), carbonates (Morris et al., 2010), aeolian dunes exhibiting cross-bedding (Hayes et al., 2011), and conglomerates with centimetre-size rounded clasts (Williams et al., 2013).

The high-cost of planetary rover missions limits risk-taking. This constraint is further compounded by limited autonomy that requires time-consuming intervention of Earth-based operators to ensure safe operations in unexplored areas. There is up to a 40 min signal delay between Earth and Mars. Furthermore, line of sight communication windows are typically limited to only a few minutes for day, exclusively during daytime. For example, the operation cycle of the Mars Exploration Rovers Spirit and Opportunity was 4 days in length: one day each for panoramic image capture, target definition upload from the ground crew, traverse to the selected target and, finally, science measurements (Erickson et al., 2002). The result is a frequently idle rover that misses potential scientifically valuable targets due to a lack of knowledge about its current surroundings. To enhance productivity, there would be added benefit if geological investigation could be undertaken with minimum human assistance.

* Corresponding author.

E-mail address: helia.sharif@carleton.ca (H. Sharif).

There has been interest in rover-based autonomous geology, mainly for obstacle detection and path planning (Maimone et al., 2006; Gor et al., 2001; Gulick et al., 2001). The Onboard Autonomous Science Investigation System (OASIS) developed by the Jet Propulsion Laboratory uses greyscale images to autonomously evaluate rocks and, on the basis of this evaluation, to acquire additional images to optimize rover resources in the navigation phase (Estlin et al., 2007). A few researchers have tried to go beyond the goal of mobility and attempted to distinguish between different types of obstacles via their colour and shape for scientific purposes (Gallant et al., 2013; Gallant, 2011). McGuire and co-workers (2004, 2010) developed the “cyber astrobiologist”, a wearable computer equipped with video which is capable of low-level geological image analysis autonomously. This system exploits the concept of metonymy in which the juxtaposition of different geological units in the key to scientific interest. As such, it is mainly trained to recognize geological contacts. Halatci and co-workers (2008) fused visual and terramechanics data to gather geological information along a rover's path.

Although rovers are getting more sophisticated and are instrumented with sensors such as mini-TES (thermal emission spectrometer), LIBS (laser-induced breakdown spectrometer), and infrared point spectrometers (Castano et al., 2007; Gazis and Roush, 2001), allowing them to make point measurements of specific mineral properties (Maki et al., 2012; Pedersen, 2001), their ability to use this information for autonomous decision making in real-time is limited. Enhanced autonomous capabilities are especially required after the navigation phase. This occurs when the rover is in its final approach to a target or has reached the target and needs to select specific instruments to initiate procedures for conducting scientific investigations.

2. Objectives

This paper reports on a promising approach to autonomous geoscience centered on the development of a rock classification system based on image processing using Bayesian networks (Sharif, 2013). Whereas human geologists use an extensive suite of visual cues (e.g. colour of streak on a ceramic plate, relative proportion of grains of different sizes, lustre, cleavage, etc.) and physical measurements (e.g. hardness comparisons, magnetism, etc.) to identify minerals and rocks, the proposed classification system solely relies on 2D greyscale digital images. From a catalogue of 180 images of 30 different rock samples, the system computes 13 textural parameters which are grouped into a 5-bin data structure. The local probabilities for each parameter to fall within a given bin form the evidence upon which the system, using a Bayesian approach, evaluates the overall probability of correctly classifying a rock sample. A Bayesian classification approach was first developed for the Nomad rover to detect dark meteorites against the white surface of snow in Antarctica (Wagner et al., 2001; Apostolopoulos et al., 2000). It has also been demonstrated to classify minerals from observations of features such as perimeter, dimensions, surface roughness, and colour (hue, saturation, and intensity) (Thompson et al., 2005).

The objectives of this study were: (1) to extract textural features on images of rock samples, (2) to combine these parameters in a Bayesian image analysis system to achieve a robust classification, and (3) to validate the system on a wide variety of rock samples and assess its performance. The proposed approach works independently of colour; rather, it relies on textural information to classify rock samples.

Table 1
Image acquisition parameters.

Camera model	Canon Power Shot SD780IS Digital ELPH
Camera lens	Optical Zoom 12.1 Mega Pixel
Shutter speed	1/30 s
Aperture	f/5.6
International Standards Organizations (ISO)	100
Flash	Off
Camera mode	Macro (4x digital zoom, 3–50 cm (widescreen))
Auto zoom	Off
Image resolution	4000 × 3000 pixels
Image type	Colour
Camera-target distance	50 cm

3. Methods

3.1. Image acquisition

3.1.1. Selecting rock samples

In this study, a total of 30 hand samples, representing the three types of rock (igneous, sedimentary, and metamorphic) and a variety of textures, were selected for analysis. Some of the samples were chosen because they exhibit classic features, such as basalt with vesicles (BA1) orropy pahoehoe (BA2), others because of similarities to rocks found on Mars, such as conglomerate (CG2).

3.1.2. Imaging rock samples

All images were acquired using the same setup, on the same day (Oct. 25, 2012), in order to reduce variations in ambient lighting. Imaging was done outdoors on a cloudy day to ensure a natural diffuse lighting, minimizing shadows and specular reflections. A digital camera mounted on a frame took overhead images of the samples at normal incidence, at a distance of 50 cm (Table 1). Two different surfaces of each rock sample were imaged, originally in colour. For calibration purposes, an 18% gray card was used prior to taking an image to ensure that the colour balance remained consistent.

In this proof-of-concept, a short camera-target distance was chosen to represent a scenario in which the rover is parked at a scientifically interesting site with several rocks in the immediate vicinity. The rover classifies the images to prioritize which rocks to examine before physical sampling or long integration measurements take place (e.g. alpha particle X-ray spectrometry). The approach could theoretically be extended to any arbitrary distance. However, selecting a camera-target distance too large would result in a loss of textural information. The proposed approach is therefore not meant to be used while traversing but during final approach or at a specific site.

3.1.3. Building the image library

Colour images were converted to greyscale intensity based on a weighted sum of the their red, green and blue components. The intensity varied linearly between 0 (black) and 255 (white), in incremental steps of 1. The greyscale images were stored as unsigned 8-bit integers.

Subsequently, three 256 × 256 pixels, non-overlapping subsets of each greyscale image were selected for analysis (Fig. 1). Since two images of each sample were taken, this leads to a library of 6 images per sample (Fig. 2). Each image covers a 3.5 × 3.5 cm² area on the sample's surface.

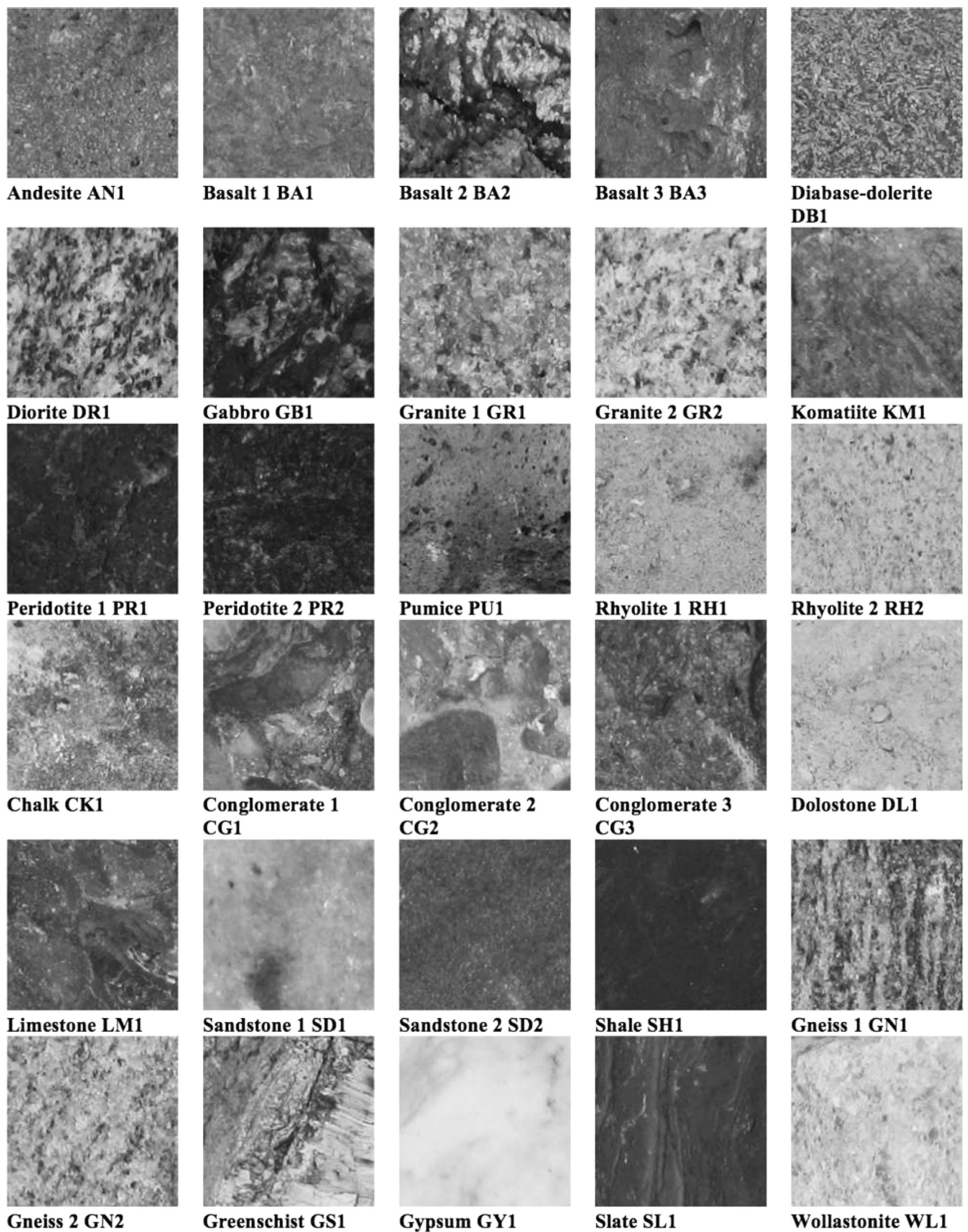


Fig. 1. Image library (one image of each rock sample is shown). Each image has a resolution of 256 × 256 pixels, and 256 gray levels.

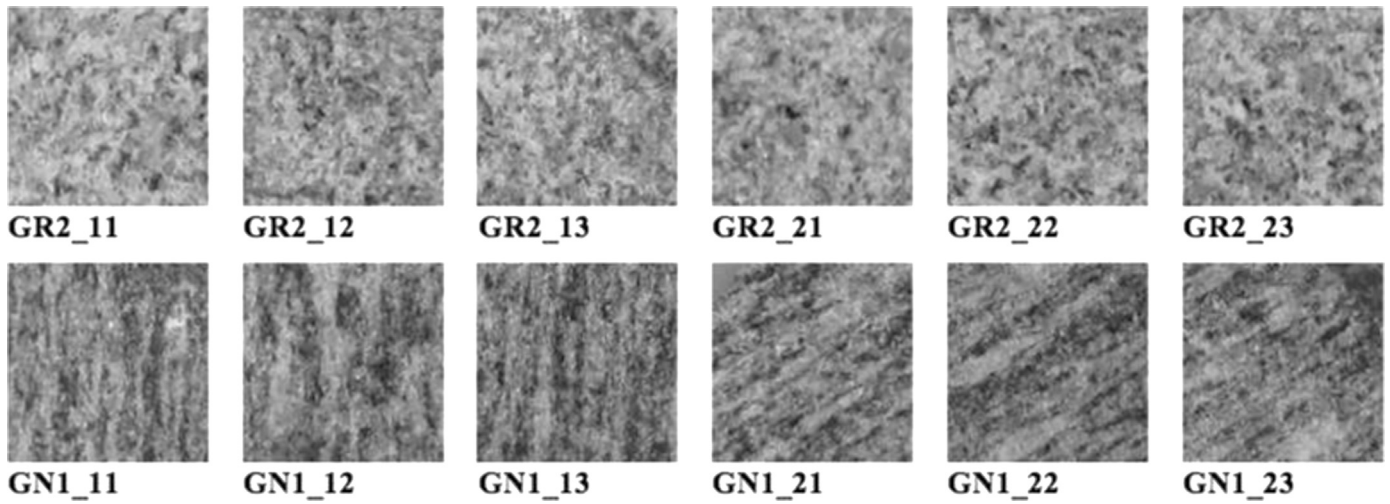


Fig. 2. Examples of 6 non-overlapping images for 2 rock samples: granite (GR2) (top row), gneiss (GN1) (bottom row).

3.2. Textural feature extraction

3.2.1. Gray level co-occurrence matrices

Simple shape-related metrics, such as the maximum average, standard deviation, and skewness of the intensity distribution did not provide enough discrimination between the grayscale digital images of the different rock samples. Firstly, the number of these shape-related metrics is limited. Secondly, and more importantly, in operational conditions, the maximum and average intensity will vary according to lighting conditions, which is undesirable. Finally, the standard deviation and skewness of the intensity distribution are unaffected by the spatial distribution of pixels with different intensities, and can be the same for vastly different samples, which is also problematic (González et al., 2009). This is illustrated in Fig. 3 for granite and gneiss which both feature the same mineral assemblage (feldspar, mica, quartz). The minerals, however, are distributed differently in these two rocks: they are randomly distributed in granite; they are organized in light and dark compositional bands in gneiss. The standard deviation and skewness are not capable of distinguishing this critical textural difference. To avoid these problems – that is, to increase the number of parameters usable, to reduce sensitivity to variations in lighting, and to capture texture – a more advanced feature extraction technique based on Haralick parameters (Haralick, 1979; Haralick et al., 1973) and widely used for classification of satellite images (Tsaneva, 2008; Haralick and Shanmugam, 1974) was utilized.

The first step in the Haralick feature extraction technique is the computation of the Gray Level Co-occurrence Matrix (GLCM). The GLCM counts the number of times adjacent pixels have the same intensity. It is configured to perform four scans of an image: along the horizontal axis (0° angle), the diagonal axis (45° angle), the vertical axis (90° angle) and the cross-diagonal axis (135° angle) (Fig. 4). Counts of similar intensities cluster diagonally on the GLCM, whereas abrupt intensity variations plot further away from the diagonal line. Since the grayscale used in this study has 256 levels, each of the 4 GLCMs associated to an image has a dimension of 256×256 elements, with coordinates i and j ranging from 0 to 255. The top left and bottom right corners of the GLCMs correspond to dark and light pixel pairs, respectively.

Fig. 5 shows the GLCMs of granite image GR2_13 and gneiss image GN1_11 shown in Fig. 2. As expected from its “salt and pepper” appearance, the GLCMs for granite image GR2_13 have a larger number of adjacent pixels with different intensities. The higher count values are shifted towards darker pixels. On the other hand, the GLCMs for the banded gneiss image GN1_11 have higher counts in a narrow band along the diagonal, corresponding to a frequent occurrence of adjacent pixels of same intensity. The higher count values are skewed towards lighter pixels.

In this study, we averaged the 0° , 45° , 90° , 135° GLCMs. As exemplified by Fig. 6, averaged GLCMs provide a rich source of discriminatory information that will be exploited in the calculation of Haralick parameters.

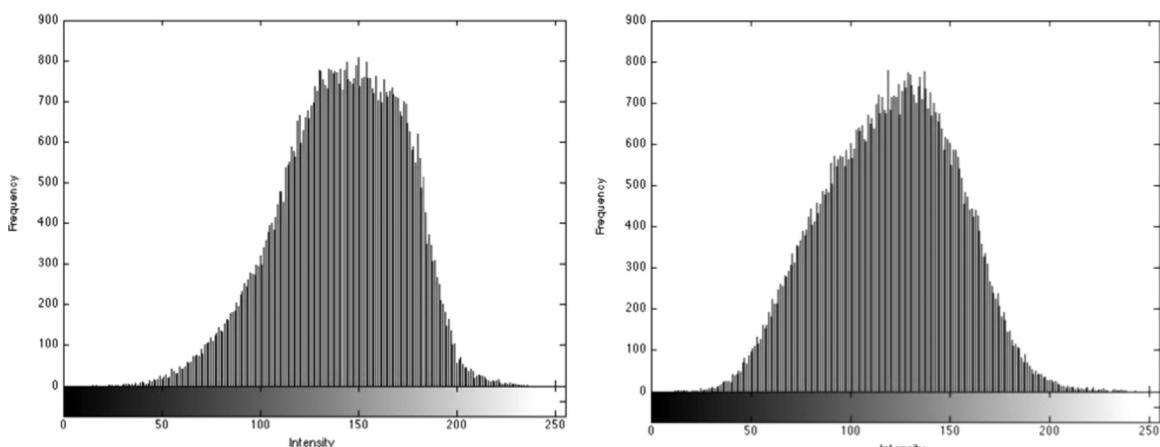


Fig. 3. Intensity distribution histograms for samples granite (left: GR2_13), and gneiss (right: GN1_11). The maximum, average, standard deviation, and skewness of the intensity is 236.00, 141.37, 30.96, and 0.72 for the granite, and 243.00, 120.26, 32.91, and 0.57 for the gneiss.

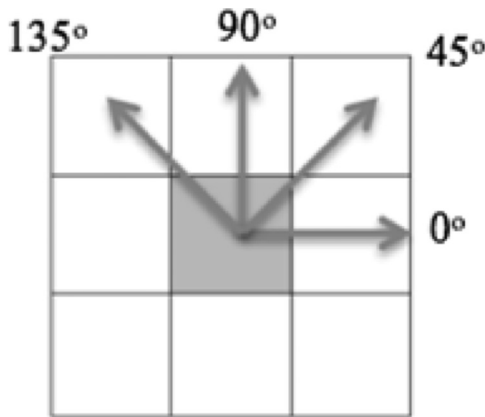


Fig. 4. GLCM scanning pattern.

3.2.2. Haralick parameters

Haralick et al. (1973) originally defined 14 parameters that can be calculated from the GLCMs (Table A1 and A2). Gotlieb and Kreysig (1990) subdivided the parameters in four categories: those expressing visual textural characteristics (f_1, f_2, f_3), those based on simple statistics ($f_4, f_5, f_6, f_7, f_{10}$), those based on information theory (f_8, f_9, f_{11}), and those based on information measures of correlation (f_{12}, f_{13}, f_{14}). From Table A1 and A2, five groups of closely related parameters can be defined:

- Large-scale homogeneity descriptors: $f_1, f_5, f_{10}, -f_2$
- Cluster descriptors: f_4, f_6, f_7
- Simple entropy parameters: f_8, f_9, f_{11}
- Entropy ratios: f_{12}, f_{13}
- Linear correlation descriptor: f_3

We computed Haralick parameters f_1 to f_{13} , and presented results as bar graphs (Figs. 7–9). Parameter f_{14} was not used because of its high computational demand in view of the limited computer power typically available on an exploration rover. For example, the computer of the most recent Mars exploration rover, Mars Science La-

batory (MSL), has a 200 MHz clock, 256 Mbytes of random-access memory and 512 Mbytes of flash memory (Bajracharya et al., 2008).

Figs 7 to 9 show bar graphs for parameters f_1, f_2 and f_3 which can be interpreted based on visual characteristics, for the complete image library. Short bars indicate that, for a given parameter, the 6 images of the same sample gave very consistent results. Larger bars denote more variability. Parameter f_1 describes homogeneity on the scale of the whole image. For this reason, the uniformly dark coarse-grained gabbro (GB1) has a higher f_1 value than diorite (DR1) which is composed of alternating plagioclase (light) and amphibole or biotite (dark). Conversely, parameter f_2 is sensitive to abrupt intensity variations. Diorite (DR1) has therefore a higher f_2 value than gabbro (GB1). Parameter f_3 detects linear trends in an image. Gneiss (GN1) has more abrupt variations between white and black bands and therefore a high f_3 value, whereas granite (GR2) has a lower f_3 value associated with gradual changes from light gray (feldspar) to darker gray (quartz) to black (mica).

3.2.3. Member functions

A data structure based on member functions was defined to group parameter values. The purpose of this binning system is to build a catalogue for each parameter, which is later used to calculate Bayesian probabilities. For each parameter, the values for each of the 6 images (represented as single bars in Figs. 7–9) of a given rock sample are averaged. The resulting 30 data points are then distributed into five bins (low, low–medium, medium, medium–high, high) using three Gaussian functions in the centre, flanked by two sigmoidal functions on either side (Fig. 10). The Gaussian and sigmoidal functions are calculated as

$$y = \exp\left(-\frac{(x - \psi)^2}{2\phi}\right) \quad (1)$$

and

$$y = \frac{1}{1 + \exp(-a(x - c))} \quad (2)$$

where

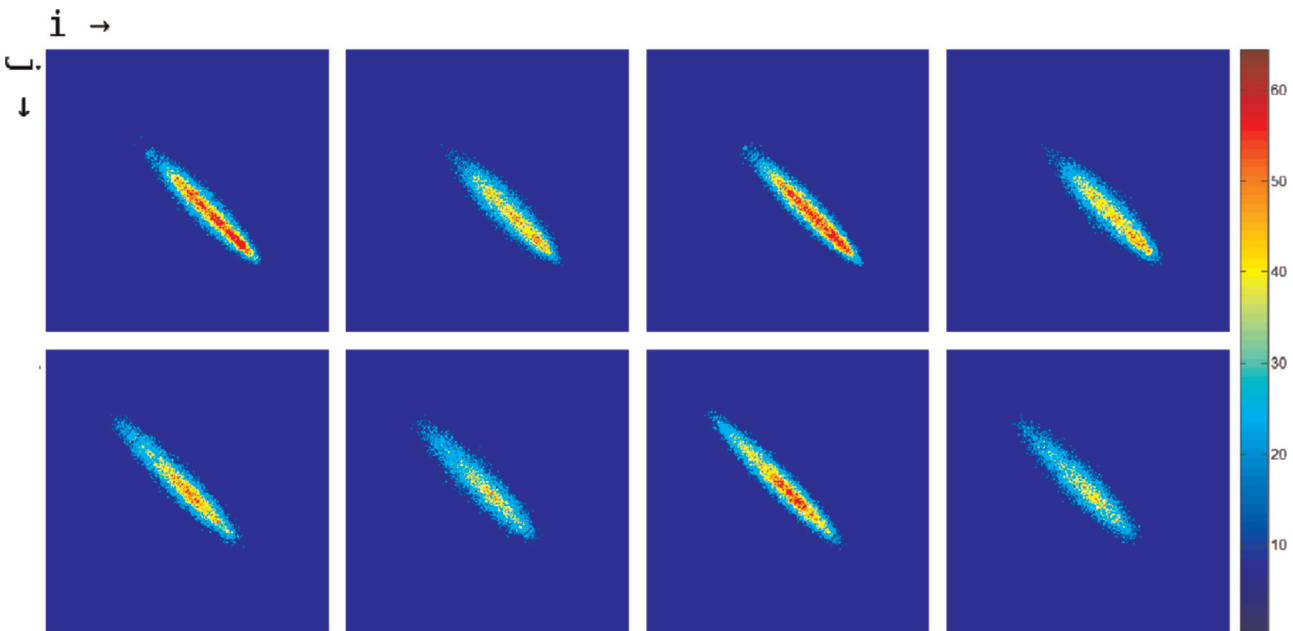


Fig. 5. GLCMs for images granite GR2_13 (top row) and gneiss GN1_11 (bottom row), and scan angles 0°, 45°, 90°, and 135°, from left to right. Letters i and j are the column and row indices, respectively.

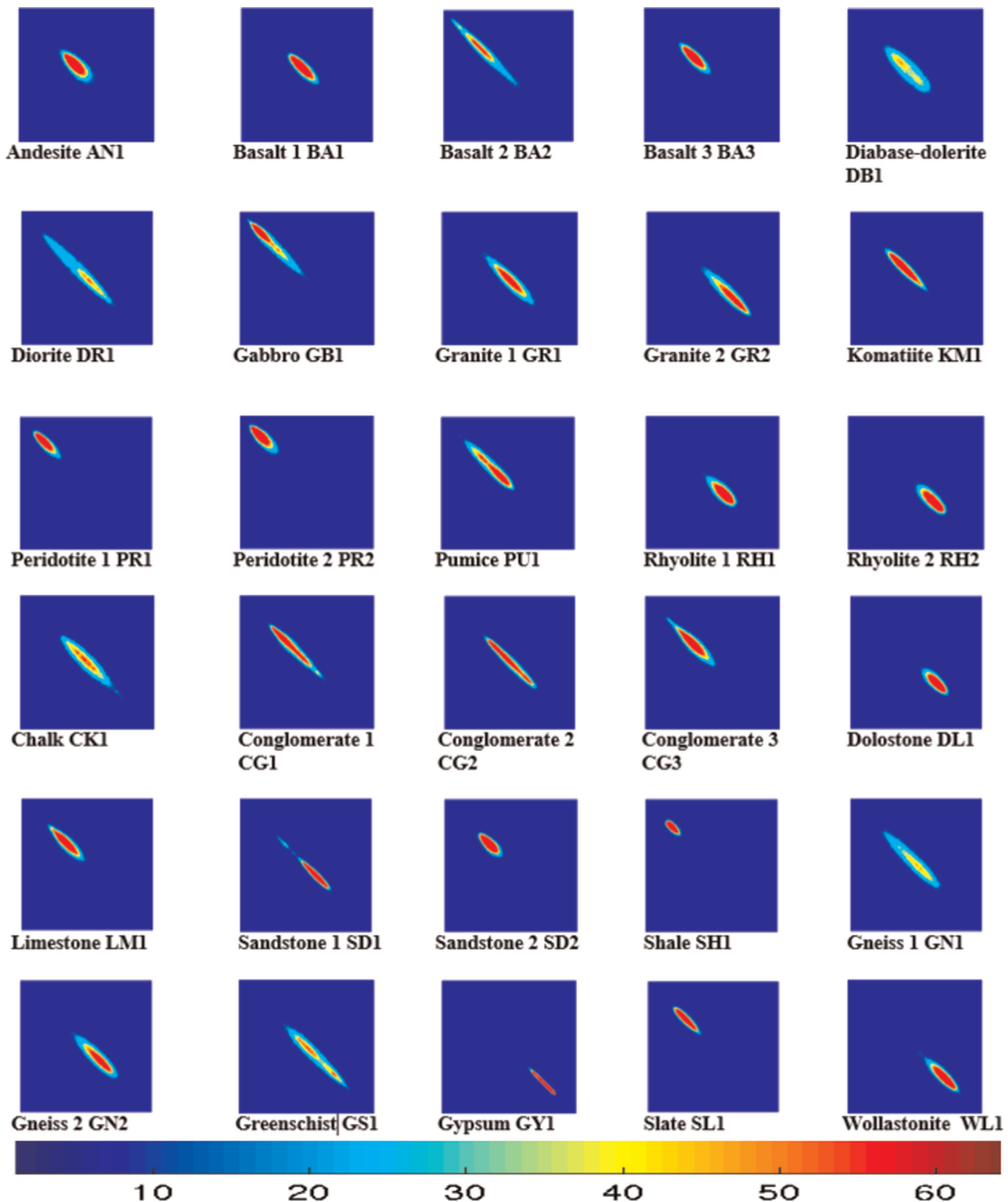
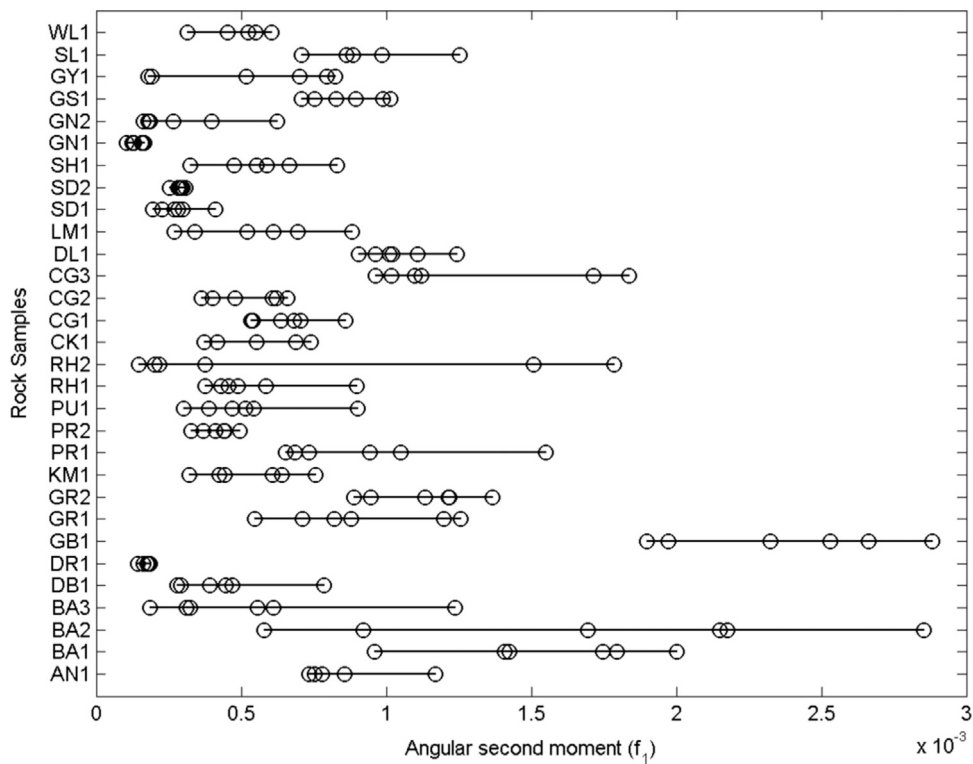
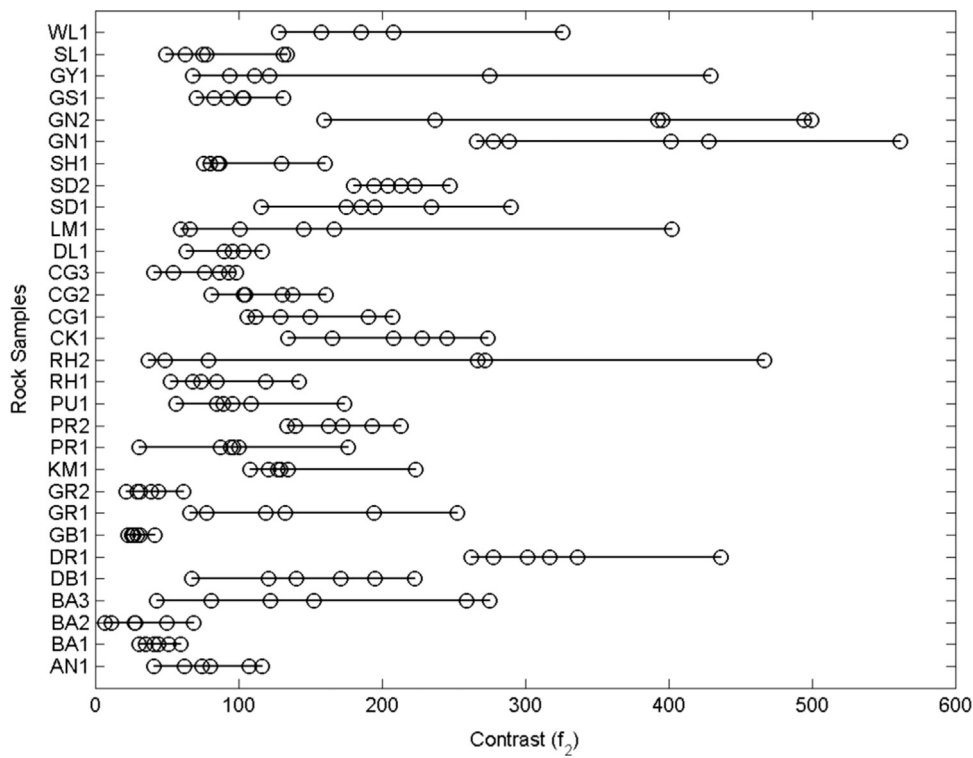


Fig. 6. Averaged GLCMS for the images shown in Fig. 1.

**Fig. 7.** Angular second moment (f_1).**Fig. 8.** Contrast (f_2).

and

$$a = \frac{\log \left(\left(\frac{1}{v} - 1 \right) / \left(\frac{1}{1-v} - 1 \right) \right)}{n\phi} \quad (3) \quad c = \Psi \pm \sqrt{2\phi^2 \log(2)} \quad (4)$$

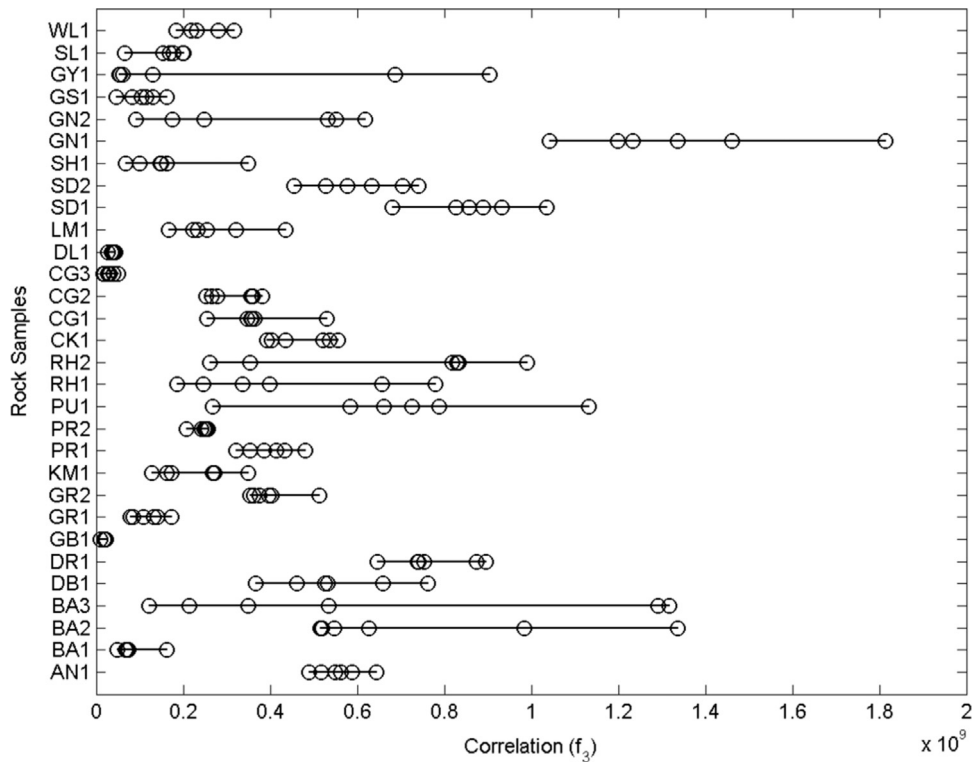
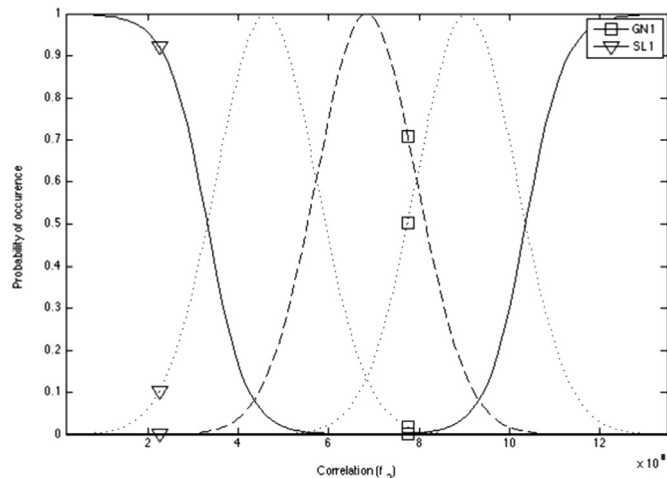
Fig. 9. Correlation (f_3).

Fig. 10. 5-bin data structure based on a central (dashed line) and two side (dotted lines) Gaussian functions, and two sigmoidal (solid lines) functions for parameter correlation (f_3). In this example, gneiss (GN1) is assigned a value of 0.00 in the low bin, 0.02 in the low–medium bin, 0.71 in the medium bin, 0.50 in the medium–high bin, and 0.00 in the high bin. The corresponding values for slate (SL1) are 0.92, 0.10, 0.00, 0.00, and 0.00. In the catalogue for parameter f_3 , gneiss (GN1) and slate (SL1) therefore fall in the medium bin and the low bin, respectively.

For all functions, $\Phi = \sigma/2$, where σ is the standard deviation of Haralick parameter of interest. For the central Gaussian function, $\Psi = \mu$, where μ is the mean of the Haralick parameter of interest. For the side Gaussian functions and sigmoidal functions, $\Psi = \mu \pm \sigma$. The variable ν is the percentage of results that lie within the range of uncertainty of the distribution. The output y is a probability of occurrence between 0 and 1.

3.3. Bayesian image analysis

A framework based on Bayes' theorem was introduced to

determine the probability of a classification being correct. Expressed mathematically:

$$P(A|B) = P(B|A)*P(A)/P(B) \quad (5)$$

where $P(A)$ and $P(B)$ are the probabilities of events A and B respectively, and $P(A|B)$ and $P(B|A)$ are the associated conditional probabilities. The probability of a classification being correct, also known as the "posterior", is $P(A|B)$. The "prior" $P(A)$ describes the probability that classification A is correct without any conditions B; $P(A) = 1/n$ where n is the number of identification possibilities. In this study, there will always be a $P(A) = 1/30$ chance that a sample is correctly classified. $P(B)$, also termed "evidence", gives the probability of a condition being true, independent of sample classification. $P(B|A)$, often referred to as "likelihood", describes the probability of classifying a sample in a bin given an imposed result for A (i.e. true or false). For example, Equation (5) tailored to calculate the probability of an image of gneiss GN1 to fall in the medium bin for parameter correlation (f_3) becomes:

$$P(\text{gneiss=true}|f_3 = \text{medium}) = P(f_3 = \text{medium}|\text{gneiss=true})/30 \\ (P(f_3 = \text{medium}|\text{gneiss=true}) + P(f_3 = \text{medium}|\text{gneiss=false})) \quad (6)$$

The ability of the classifier to correctly identify a rock is verified by testing the catalogued samples against themselves. Each sample is checked against every member of the catalogue. The probabilities for each classification are output in a row (Table 2). A square matrix of classification probabilities is generated. Ideally, this matrix would converge to Kronecker's delta: every rock should conclusively be classified as itself and never as something else, and thus the matrix should be composed of ones on the diagonal and of zeroes off the diagonal.

4. Results

The classification results presented in Table 2 can be interpreted

Table 2

Bayesian posterior probabilities using 13 Haralick parameters. Diagonal entries are in bold.

	AN1	BA1	BA2	BA3	DB1	DR1	GB1	GR1	GR2	KM1	PR1	PR2	PU1	RH1	RH2	CK1	
Catalogued samples to identify	AN1	1.0000	0.0000	0.0000	0.0000	0.9910	0.0000	0.0000	0.0470	0.0000	0.9142	0.0000	0.0000	0.3664	0.0146	0.0000	0.0000
	CG1	CG2	CG3	DL1	LM1	SD1	SD2	SH1	GN1	GN2	GS1	GY1	SL1	WL1	Classification accuracy score		
	AN1	0.0000	0.0000	0.9999	0.0000	0.9991	0.0000	0.5777	0.0000	0.0000	0.0001	0.0000	0.0000	0.0000	0.0000	1.0	
BA1	0.0000	0.0000	0.0000	0.0000	0.0023	0.0000	0.0000	0.0000	0.0000	0.0000	0.0000	0.0000	0.0000	0.0000	0.0000	1.0	
BA2	0.0002	0.0000	1.0000	0.0000	1.0000	0.0000	0.0000	0.0000	0.0000	0.0000	0.0003	0.0000	0.0000	0.0000	0.0000	0.6	
BA3	0.0000	0.0000	0.0005	0.0000	0.9873	0.0000	0.0000	0.0000	0.0000	0.0000	0.0000	0.0000	0.0000	0.0000	0.0000	0.9	
DB1	0.0000	0.0000	1.0000	0.0000	0.9983	0.0000	0.0000	0.0000	1.0000	0.0242	0.0033	0.0000	0.0000	0.0000	0.0000	0.6	
DR1	0.0000	0.0587	0.3636	0.0000	0.0000	0.0000	0.0000	0.0000	1.0000	1.0000	1.0000	0.0000	0.0000	0.0000	0.0000	0.5	
GB1	1.0000	0.0000	0.8248	0.0000	0.9981	0.0000	0.0000	0.0000	0.0000	0.0000	0.0000	0.0000	0.0000	0.0000	0.0000	0.7	
GR1	0.0000	0.0000	0.0011	0.0000	0.0000	0.0000	0.0000	0.0000	1.0000	1.0000	1.0000	0.0000	0.0000	0.0000	0.0000	0.6	
GR2	0.0000	0.9962	0.0000	0.0000	0.0000	0.0000	0.0000	0.0000	1.0000	1.0000	1.0000	0.0000	0.0000	0.0000	0.0000	0.4	
KM1	0.0000	0.0000	0.0706	0.0000	0.3643	0.0000	0.0000	0.0000	0.0000	0.0000	0.0000	0.0000	0.0000	0.0000	0.0000	0.0	
PR1	0.0000	0.0000	0.0030	0.0000	0.9999	0.0000	1.0000	0.0000	0.0000	0.0000	0.0000	0.0000	0.0000	0.1063	0.0000	0.6	
PR2	0.0000	0.0000	0.0000	0.0000	0.9822	0.0000	0.9999	0.0000	0.0000	0.0000	0.0000	0.0000	0.0000	1.0000	0.0000	0.6	
PU1	0.0000	0.0000	0.0706	0.0000	0.3643	0.0000	0.0000	0.0000	0.0000	0.0000	0.0000	0.0000	0.0000	0.0000	0.0000	0.5	
RH1	0.0000	0.0000	0.0000	0.9942	0.0000	0.0000	0.0000	0.0000	0.0000	0.8512	0.0002	0.0000	0.0000	0.0000	0.0000	0.8	
RH2	0.0000	0.0000	0.0000	0.7343	0.0000	0.0000	0.0000	0.0000	0.0000	1.0000	0.6005	0.0000	0.0000	0.0000	0.0000	0.4	
CK1	0.0000	0.0000	0.0000	0.0776	0.0000	0.0000	0.0000	0.0000	0.0000	1.0000	0.9975	0.0000	0.0000	0.0000	0.0000	0.8	
CG1	1.0000	0.0000	0.0000	0.0000	0.0000	0.0000	0.0000	0.0000	0.0000	0.0000	0.1268	0.0000	0.0000	0.0000	0.0000	0.9	
CG2	1.0000	1.0000	0.0000	0.0000	0.0000	0.0000	0.0000	0.0000	0.9845	1.0000	0.0000	0.0000	0.0000	0.0000	0.0000	0.8	
CG3	0.0000	0.0000	1.0000	0.0000	1.0000	0.0000	0.0000	0.0000	0.0000	0.0000	0.0000	0.0000	0.0000	0.0000	0.0000	0.7	
DL1	0.0000	0.0000	0.0000	1.0000	0.0000	0.9925	0.0000	0.0000	0.0000	0.0001	0.0000	0.0000	0.0000	0.0000	0.0000	0.7	
LM1	0.0000	0.0000	0.8760	0.0000	0.9755	0.0000	0.0000	0.0000	0.0000	0.0000	0.0000	0.0000	0.0000	0.0000	0.0000	0.5	
SD1	0.0009	0.8208	0.0000	1.0000	0.0000	1.0000	0.0000	0.0000	0.0000	0.0000	0.0000	0.0000	0.0000	0.0000	0.0000	0.8	
SD2	0.0000	0.0000	0.9946	0.0000	1.0000	0.0000	1.0000	0.0000	0.0000	0.0000	0.0000	0.0000	0.0000	0.0000	0.0000	0.6	
SH1	0.9952	0.0000	0.0000	0.0016	1.0000	0.0000	1.0000	0.0000	0.0000	0.0000	0.8512	0.0002	0.0000	0.0000	0.0000	0.3	
GN1	0.0000	0.0000	0.9999	0.0000	0.1693	0.0000	0.0000	0.0000	1.0000	0.9995	0.9985	0.0000	0.0000	0.0000	0.0000	0.6	
GN2	0.0000	0.0000	0.0000	0.0000	0.0000	0.0000	0.0000	0.0000	0.9995	0.9493	0.0000	0.0000	0.0000	0.0000	0.0000	1.0	
GS1	0.0000	0.0032	0.0000	0.0000	0.0000	0.0000	0.0000	0.0000	0.0000	0.9967	0.9997	0.0000	0.0000	0.0000	0.0000	1.0	
GY1	1.0000	1.0000	0.0000	1.0000	0.0000	1.0000	0.0000	0.0000	0.0000	0.0004	0.1538	1.0000	1.0000	1.0000	0.4		
SL1	0.9991	0.0000	0.0000	0.0000	0.0000	0.9996	0.0000	1.0000	0.0000	0.0000	0.0000	1.0000	0.0000	0.0000	1.0000	0.4	
WL1	0.0000	0.0000	0.0000	1.0000	0.0000	1.0000	0.0000	0.0000	0.0000	0.0007	0.0000	0.0000	0.0000	1.0000	0.8		
														TOTAL	19.5		

using the original images (Fig. 1) and the averaged GLCMs (Fig. 6). When two rocks have similar GLCMs, such as the two peridotites PR1 and PR2, the classifier confuses them and yields a false positive

(1.000). The two sandstones in question are texturally similar. Both rocks would be given the same first-order classification by a human geologist; the confusion is therefore not surprising. Two rocks having

Table 3

Bayesian posterior probabilities for 23 uncatalogued samples using 13 Haralick parameters. Diagonal entries are in bold.

.	AN1	BA1	BA2	BA3	DB1	DR1	GB1	GR1	GR2	KM1	PR1	PR2	PU1	RH1	RH2	CK1		
Uncatalogued samples to identify	AN1	1.00000	0.00000	0.00000	0.00000	0.0591	0.00000	0.00000	0.05460	0.00000	0.9261	0.00000	0.00000	0.40520	0.00000	0.0000		
BA1	0.00000	0.99990	0.00000	0.99620	0.00000	0.00000	0.00000	0.00000	0.00080	0.00000	0.00000	0.00340	0.00000	0.00000	0.00000	0.0000		
BA2	0.00000	0.00521	0.00000	0.9127	0.00000	0.0001	0.00000	0.00000	0.00001	0.00000	0.00000	0.00000	0.00000	0.00000	0.00000	0.0000		
BA3	0.00001	0.00000	0.00001	0.00000	0.00000	0.00000	0.00010	0.00000	0.00000	0.24571	0.00001	0.00000	0.00920	0.00000	0.00000	0.0000		
DB1	1.00000	0.00000	0.4713	0.00001	1.00000	0.00000	0.00001	0.00000	0.00000	0.97740	0.00000	0.00000	0.34040	0.00000	0.00000	0.0000		
DR1	0.00000	0.00000	0.00000	0.00000	0.92841	0.00000	0.00001	0.00001	0.00000	0.00560	0.00000	0.00000	0.22400	0.00000	0.00000	1.0000		
GB1	0.00000	0.48661	0.00000	0.98950	0.00000	0.00001	1.00000	0.00000	0.00000	0.00000	0.00000	0.00000	0.95780	0.00000	0.00000	0.0000		
GR1	0.00030	0.00000	0.00000	0.00000	0.00000	0.00000	0.00001	1.00000	0.00000	0.00040	0.00000	0.00000	0.04130	0.00000	0.00002	0.9992		
GR2	0.00000	0.00000	0.00000	0.00000	0.00001	0.00000	0.00001	0.00001	1.00000	0.00000	0.00000	0.00000	0.00520	0.00001	0.6798	1.0000		
KM1	0.00000	0.00000	0.00020	0.00000	0.00000	0.00000	0.00000	0.00001	0.00000	0.94420	0.00000	0.00000	0.60190	0.00000	0.00000	0.0000		
PR1	0.00001	0.00000	0.0415	1.00000	0.00000	0.00000	0.00000	0.2101	0.00000	0.00000	0.48161	0.00001	0.00000	0.00950	0.00000	0.0000		
PR2	0.00001	0.00000	0.00411	1.00000	0.00000	0.00000	0.91200	0.00000	0.00000	0.04441	0.00001	1.00000	0.00000	0.00050	0.00000	0.0000		
PU1	0.00000	0.00000	0.00000	0.00000	0.00000	0.00000	0.00000	0.00000	0.00000	0.34930	0.00000	0.00000	0.4165	0.00000	0.00000	0.0000		
RH1	0.3145	0.00000	0.00000	0.00000	0.00000	0.00000	0.00000	0.00000	0.00000	0.00000	0.00000	0.00000	0.00001	1.00000	1.0000	1.0000		
RH2	1.00000	0.00000	0.00000	0.00000	0.00000	0.00000	0.00001	0.00001	0.00000	0.00000	0.00000	0.00000	0.00051	0.00001	1.00000	1.0000		
CK1	0.1464	0.00000	0.00000	0.00000	0.00000	0.00000	0.00000	0.00000	0.00000	0.00000	0.00000	0.00000	0.00000	0.00000	0.6619	0.0000		
CG1	0.00000	0.00000	0.00000	0.00000	0.00000	0.00000	0.00000	0.00000	0.00000	0.00000	0.00000	0.00000	0.00000	0.00000	0.00000	0.0000		
CG2	0.00000	0.00000	0.00000	0.00000	0.00000	0.00000	0.00000	0.00000	0.00000	0.00000	0.00000	0.00000	0.00037	0.00000	0.00000	0.0000		
CG3	0.99930	0.00001	0.00000	0.0115	0.00000	0.00000	0.05440	0.00200	0.00001	0.00000	0.00000	0.00000	0.98520	0.00000	0.00000	0.0000		
DL1	0.00000	0.00000	0.00000	0.00000	0.00000	0.00000	0.00000	0.00000	0.00000	0.00000	0.00000	0.00000	0.99990	0.00000	0.9681	0.0000		
LM1	0.00010	0.42020	0.99950	0.99360	0.00000	0.00000	0.74440	0.00000	0.00000	0.99980	0.00000	0.00000	0.89340	0.00000	0.00000	0.0000		
SD1	0.00000	0.00040	0.00000	0.00000	0.00000	0.00000	0.00000	0.00000	0.00000	0.00000	0.00000	0.00000	0.00000	0.00000	0.00001	0.0000		
SD2	1.00000	0.99970	0.04891	0.00000	0.00000	0.00000	0.00000	0.00000	0.00000	0.96451	0.00000	0.99920	0.02520	0.00010	0.00000	0.0000		
CG1	CG2	CG3	DL1	LM1	SD1	SD2	SH1	GN1	GN2	GS1	GY1	SL1	WL1	Classification accuracy score				
AN1	0.00000	0.00000	0.99990	0.00000	0.99860	0.00000	0.00000	0.00000	0.00000	0.00000	0.00000	0.00000	0.00000	0.00001				
BA1	0.00000	0.00000	0.00000	0.00000	0.00230	0.00000	0.00000	0.00000	0.00000	0.00000	0.00000	0.00000	0.00000	0.00001				
BA2	0.0148	0.00001	0.00000	0.00001	0.00000	0.00000	0.00000	0.00000	0.00000	0.00020	0.00000	0.00000	0.00000	0.00000	0.6			
BA3	0.00000	0.00000	0.00030	0.00000	0.99910	0.00000	0.99990	0.00000	0.00000	0.00000	0.00000	0.00000	0.00400	0.00000	0.00007			
DB1	0.00000	0.00001	0.00000	0.00000	0.99830	0.00000	0.00000	0.00001	0.00000	0.02420	0.00330	0.00000	0.00000	0.00000	0.6			
DR1	0.00000	0.47560	0.02000	0.00000	0.00000	0.00000	0.00000	0.00001	0.00001	0.00000	0.00000	0.00000	0.00000	0.00000	0.4			
GB1	0.98030	0.00000	0.99860	0.00000	0.99930	0.00000	0.00000	0.00000	0.00000	0.00000	0.00000	0.00000	0.00000	0.00000	0.00008			
GR1	0.00000	0.00000	0.0011	0.00000	0.00000	0.00000	0.00000	0.00001	0.00001	0.00000	0.00000	0.00000	0.00000	0.00000	0.00006			
GR2	0.00000	0.99620	0.00000	0.00000	0.00000	0.00000	0.00000	0.00000	0.00000	0.00001	0.00001	0.00000	0.00000	0.00000	0.00004			
KM1	0.00000	0.00000	0.79290	0.00000	0.29240	0.00000	0.00000	0.00000	0.00000	0.00040	0.00080	0.00000	0.00000	0.00000	0.00005			
PR1	0.00000	0.00000	0.00300	0.00000	0.99990	0.00001	0.00000	0.00000	0.00000	0.00000	0.00000	0.00000	0.1063	0.00000	0.6			
PR2	0.00000	0.00000	0.00000	0.00000	0.91710	0.00000	0.99970	0.0136	0.00000	0.00000	0.00000	0.00000	0.00001	0.00000	0.00006			
PU1	0.00000	0.00000	0.04000	0.00000	0.1756	0.00000	0.00000	0.00000	0.00000	0.00000	0.00000	0.00000	0.00000	0.00000	0.00005			
RH1	0.00000	0.00000	0.00000	0.99600	0.00000	0.00000	0.00000	0.00000	0.00000	0.00000	0.00000	0.00000	0.00000	0.00000	0.00008			
RH2	0.00000	0.00000	0.00000	0.73430	0.00000	0.00000	0.00000	0.00000	0.00001	0.00000	0.00000	0.00000	0.60050	0.00000	0.00004			
CK1	0.00000	0.00000	0.00000	0.00000	0.00000	0.00000	0.00000	0.00000	0.00000	0.00000	0.00000	0.00000	0.00000	0.00000	0.00000			
CG1	0.99800	0.2133	0.00000	0.00000	0.00000	0.00000	0.00000	0.00000	0.00000	0.00000	0.0290	0.70390	0.00000	0.00000	0.00001			
CG2	0.99991	0.00000	0.00001	0.00000	0.00000	0.00000	0.00000	0.00000	0.00000	0.00000	0.00290	0.70390	0.00000	0.00000	0.00001			
CG3	0.00000	0.00001	0.00000	0.00000	0.00000	0.00000	0.00000	0.00000	0.00000	0.00000	0.00000	0.00000	0.00000	0.00000	0.00000	0.7		
DL1	0.00000	0.00000	0.00000	0.00001	0.00000	0.00000	0.00000	0.00000	0.00000	0.00000	0.00000	0.00000	0.00000	0.00001	0.00000	0.9		
LM1	0.00000	0.00000	0.99970	0.00000	0.00001	0.00000	0.00000	0.00000	0.00000	0.00000	0.00000	0.00000	0.00000	0.00000	0.00001	0.00000	0.9	
SD1	0.00000	0.1850	0.00001	0.00000	0.00000	0.00000	0.00000	0.00000	0.00000	0.00000	0.00000	0.00000	0.00000	0.00001	0.00000	0.8		
SD2	0.00000	0.00000	0.99460	0.00001	0.00000	0.00000	0.00000	0.00000	0.00000	0.00000	0.00000	0.00000	0.00000	0.00000	0.00000	0.00000	0.6	
														TOTAL	15.5			

different visual aspect and GLCMs are generally not confused; for example, the GLCM of pumice (PU1) has a much more elliptic shape than that of sandstone (SD2), which gives an unequivocal null result. A complication arises when two geologically dissimilar rocks are confused. For example, slate (SL1) is confused with basalt (BA1), gabbro (GB1), peridotite (PR1 and PR2) and shale (SH1); a likely cause if that all of these rocks are dark with insufficient contrast for the classifier. A simple empirical scoring system was devised to quantify classification accuracy. In practice, within each row of the classification matrix, the diagonal entry should be the maximum, or at least be above a certain threshold. Furthermore, values above this threshold should not be repeated throughout the row. For each row in Table 2, a correct classification (probability of 1.000 along the diagonal) was therefore assigned 1.0 point; 0.5 points were subtracted if the probability of classification was too low

(< 0.9900); and 0.1 points were subtracted for each false positive. If the diagonal entry was not the maximum of the row, no points were given. The possible score for a single row ranges from 0 to 1; negative scores were capped at 0. The total score for the whole matrix is reported in the bottom right corner of Table 2 and is equal to 19.5/30 points (65%).

The robustness of the classifier was verified using 23 uncatalogued samples. These samples are images of the same rocks as shown in Fig. 1. The rocks selected were physically large enough so that 6 additional non-overlapping digital images of their surface could be acquired, under the same lighting conditions. The corresponding images were not, however, included in the computation of the bar graphs and the 5-bin data structure. Table 3 shows the classification results for these uncatalogued samples. The classification accuracy score for the 23 rocks was very consistent:

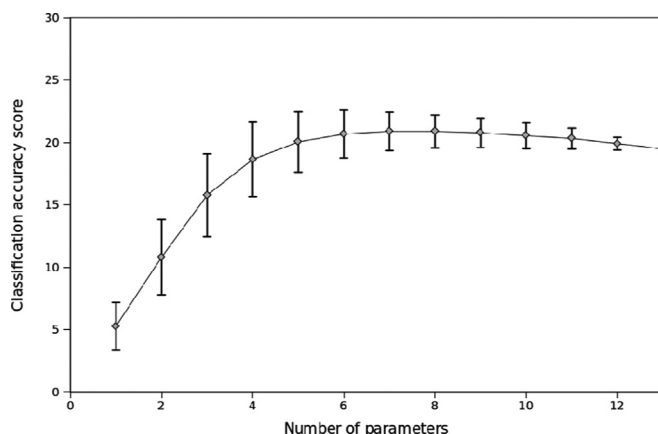


Fig. 11. Classification accuracy score versus number of Haralick parameters used in the computation of Bayesian probabilities. Error bars correspond to one standard deviation.

15.5/23 points (67.4%) for the uncatalogued samples and 15.0/23 points (65.2%) for the corresponding samples from the catalogue.

5. Discussion

As the number of parameters used in the computation of the probabilities increases, so does the number of false positives which degrades the performance of the classifier. We therefore investigated how many parameters would be optimal for increasing performance. We repeated the analysis presented in Table 2 for the 8191 ($2^n - 1$ where $n=13$) possible combinations of parameters. Fig. 11 shows how the classification accuracy is highest for 4, 5 or 6 parameters and slightly declines for a larger

number of parameters.

Since better classification results are achieved using a subset of Haralick parameters, which parameters lead the highest classification accuracy scores? Out of the 8191 possible combinations of parameters, the highest score attained was 24.1 (80.3%) and was achieved using 6 Haralick parameters: f_1 , f_2 , f_3 , f_4 , f_{10} , and f_{13} (Tables 4 and 5). For 24 of the 25 highest scores, 4, 5 or 6 parameters were used as predicted in Fig. 11. The Haralick parameters used the most are f_3 and f_{13} (used 18 times) and f_1 and f_5 (used 13 times). It is interesting to note that these four parameters fall in 3 of the 4 categories defined in section 4.2 above. It seems that a combination of parameters which describe images using different perspectives are the best choice to achieve a high classification accuracy.

6. Conclusion

This paper presented a proof-of-concept for a rock classification system designed for onboard processing and autonomous decision-making on a planetary exploration rover. The classifier inputs grayscale digital images of rocks similar to those typically acquired by navigation or science cameras and outputs a probabilistic identification. In view of the limited processing power available on an exploration rover (Bajracharya et al., 2008), the image processing strategy has been kept to a minimum. It includes 4 simple steps: computation of GLCMs, extraction of Haralick parameters, catalogue building and calculation of Bayesian probabilities. Processing a 256×256 pixel image through these steps required approximately 3–4 s on a standard computer with a single Intel Core i3 processor, a 2.13 GHz clock, and 4 Gbytes of random-access memory. For this proof-of-concept, the code was written in MATLAB. The code could be optimized and parallelized in the future.

The proposed methodology could be extended to the classification of regolith. Regolith would be more challenging to classify because they exhibit less textural variability than the surface of rock samples

Table 4

The 25 highest classification accuracy scores (listed in decreasing order) with their associated Haralick parameters. An "X" indicates parameters which were used whereas a dash indicates parameters which were not used.

Classification accuracy score	Haralick parameters													Number of parameters used
	f_1	f_2	f_3	f_4	f_5	f_6	f_7	f_8	f_9	f_{10}	f_{11}	f_{12}	f_{13}	
24.1	X	X	X	X	–	–	–	–	X	–	–	–	X	6
24.1	X	X	X	X	–	–	X	–	–	X	–	–	X	6
24.0	–	–	–	X	X	–	–	–	X	–	–	–	X	4
24.0	–	–	–	–	X	–	X	–	X	–	–	–	X	4
24.0	–	–	–	–	–	X	–	–	X	X	–	–	X	4
23.9	X	–	–	–	–	X	–	–	X	–	–	–	X	4
23.9	–	–	–	–	X	X	–	–	X	–	–	–	X	4
23.9	–	X	X	X	–	–	–	–	X	X	–	–	X	6
23.9	–	X	X	–	–	X	–	X	X	X	–	–	X	6
23.8	X	–	X	X	–	–	–	–	–	–	X	–	X	5
23.8	X	–	X	–	–	X	–	–	–	X	–	X	–	5
23.8	X	–	–	–	X	–	X	–	X	–	–	–	X	5
23.8	X	–	X	–	X	–	X	X	–	–	–	X	–	6
23.7	X	–	–	–	X	–	–	X	X	X	–	–	X	5
23.7	X	X	X	X	X	–	–	–	–	–	X	–	–	6
23.7	X	X	X	–	X	–	X	–	–	–	X	–	–	6
23.7	X	–	X	X	X	–	–	X	–	–	X	–	–	6
23.7	X	–	X	X	X	–	–	X	–	–	–	X	–	6
23.7	–	X	X	X	X	–	–	X	–	–	X	–	–	6
23.7	–	–	X	X	X	–	–	X	–	X	–	X	–	6
23.7	–	–	X	–	X	–	X	X	–	X	–	X	–	6
23.7	X	X	X	–	–	X	–	X	–	X	–	–	X	7
23.6	–	–	X	X	–	–	–	–	–	–	X	–	X	4
23.6	–	–	X	–	–	X	–	–	–	X	–	–	X	4
Number of times a parameter is used		13	8	18	10	13	5	10	7	10	9	5	7	18

Table 5

Bayesian posterior probabilities using Haralick parameters f_1 , f_2 , f_3 , f_4 , f_{10} , and f_{13} . Diagonal entries are in bold.

and outcrops. Nonetheless, parameters such as the degree of compaction and grain size could express themselves visually and therefore be captured on images and be candidate for an analysis. The output of

regolith classification could be further validated by terramechanics data acquired by the rover mobility system.

The rock classification system has been demonstrated for 30 rock

samples. Further research is needed to investigate the impact of ambient lighting conditions on the original images. A way to mitigate the effects of variations in lighting could be to implement controlled illumination on the rover. Provided that strategies could be put in place to eliminate the effects of variable lighting, a very large number of images could be used. At present, methodologies have been developed to assess how many parameters and which parameters lead the highest classification accuracy scores. Using a much larger population of images would allow these preliminary results to be generalized.

The image resolution used in this study is approximately 0.1 mm/pixel which captures details that would be seen by a human geologist using a hand lens. It would be interesting to test the methodology at higher resolution (closer to that of a petrographic microscope) and at lower resolution (similar to the naked eye). The use of a grayscale with finer levels than 256 should also be tested.

This study has shown that merely adding more and more parameters into the classification system does not necessarily improve performance. Parameters must be selected with care. A mix of very different parameters is best. It would be interesting to test the usefulness of adding images taken at different wavelength as rover cameras are always fitted with filter wheels (Griffiths et al., 2005; Ellery et al., 2004; Ellery and Wynn-Williams, 2003).

Finally, the rock classification system proposed here could become a modular part of a more complex rover-based expert system for autonomous science. A candidate for integration is the Zoe rover test platform which has been demonstrated in the Atacama desert of Chile (Cabrol et al., 2007; Smith et al., 2007; Warren-Rhodes et al., 2007). The instruments onboard Zoe have mainly

been selected to search and identify biosignatures. The Zoe platform then uses a Bayesian classifier to interpret the data. The rock classification system would provide an additional stream of data to Zoe. Another example is the ASTIA system which is under development for the ExoMars mission (Woods et al., 2009). ASTIA assigns numerical values to geological attributes such as structure (e.g. shape, orientation, and form), texture (e.g. fabric lustre, grain size), and composition (e.g. colour, albedo, mineralogy) rather than attempting to perform a direct classification. It focuses on more global characteristics such as identification of geological boundaries and transitions between geological domains. Rock identification provided by the system proposed here would complement that knowledge and contribute to reduce uncertainty in geological mapping.

Acknowledgements

Ms. Beth Halfkenny, curator of the collections of the Department of Earth Sciences at Carleton University kindly provided the rock samples used in this research. Dr. Patrick Boily from the Centre for Quantitative Analysis and Decision Support at Carleton University offered expert advice on Bayesian probabilities.

Appendix A. : Haralick parameters

See Table A1 and A2

Table A.1

Definitions of Haralick parameters. Descriptions follow Haralick et al. (1973), Haralick and Shanmugam (1974), Gotlieb and Kreysig (1990), and Van der Sanden and Hoekman (2005).

Parameter	Name	Formula	Description
f_1	Angular second moment	$\sum_{i=1}^N \sum_{j=1}^N (p(i,j))^2$	Describes large-scale homogeneity: an image with similar grayscale values throughout will have a high f_1 .
f_2	Contrast	$\sum_{n=0}^{N-1} n \sum_{i=1}^N \sum_{j=1}^N p(i,j); n = i - j $	Measures how much local variation exists in an image; the more variation exists, f_2 increases. It is opposite to f_1 , i.e. low f_1 corresponds to high f_2 and vice versa.
f_3	Correlation	$\frac{\sum_{i=1}^N \sum_{j=1}^N (i\bar{j})p(i,j) - \mu_x\mu_y}{\sigma_x\sigma_y}$	Describes the linear structure of an image; a large f_3 indicates the presence of linear trends in an image.
f_4	Sum of squares variance	$\sum_{i=1}^N \sum_{j=1}^N (i - \mu)^2 p(i,j)$	A f_4 suggests that there is a range of pixel pairs, which could correspond to a sample heterogeneous at a pixel scale, or one having clear light-dark clustering. Similar to f_7 .
f_5	Inverse difference moment	$\sum_{i=1}^N \sum_{j=1}^N \frac{p(i,j)}{1 + (i-j)^2}$	Measures large-scale homogeneity like f_1 . Similar but with opposite trend to f_2 .
f_6	Sum average	$\sum_{i=1}^{2N} ip_{x+y}(i)$	Describes the most frequent adjacent pair. A high average suggests that the typical pixel pair consists of darker pixels, which can correspond to an image that has plenty of dark clusters. Similar trend to f_4 and f_7 .
f_7	Sum variance	$\sum_{i=1}^{2N} (i - f_8)p_{x+y}(i)$	Variance measure closely related to f_4 .
f_8	Sum entropy	$-\sum_{i=1}^{2N} p_{x+y}(i) \log \{p_{x+y}(i) + \epsilon\}$	Describe how much information is contained within the GLCM. As the entropy increases, so does the randomness.
f_9	Entropy	$-\sum_{i=1}^N \sum_{j=1}^N p(i,j) \log \{p(i,j) + \epsilon\}$	Same as f_8 except for $p(i,j)$ instead of p_{x+y} .
f_{10}	Difference variance	Variance of p_{x-y}	Closely related to f_5 . Measures large-scale homogeneity. It has somewhat of an opposite trend to f_4 , f_6 , and f_7 because it is computed from p_{x-y} .
f_{11}	Difference entropy	$-\sum_{i=1}^{N-1} p_{x-y}(i) \log \{p_{x-y}(i) + \epsilon\}$	Same as f_8 except for p_{x-y} instead of p_{x+y} .
f_{12}	Information measure of correlation I	$\frac{HXY - HXY_1}{\max(HX, HY)}$	Entropy-based measurement with no clear visual correlation.
f_{13}	Information measure of correlation II	$\sqrt{1 - \exp(-2(HXY_2 - HXY))}$	Similar but with an opposite trend to f_{12} .
f_{14}	Maximal correlation coefficient	Square root of the second-largest eigenvalue of Q , where $Q(i, j) = \sum_{i=1}^N \sum_{j=1}^N \sum_{k=1}^N \frac{p(i,k)p(j,k)}{p_X(i)p_Y(k)}$	Based on information theory. While given in Haralick et al. (1973), we did not use it due to its computational demands.

Table A.2

Symbols used in Table A.1.

Symbol	Formula	Comments
i, j, k	–	Matrix indices
$p(i,j)$	–	Single entry at position (i,j) in a normalized GLCM, i.e. $p = \frac{GLCM}{\sum_{i=1}^N \sum_{j=1}^N GLCM}$
$p_x(i)$	$\sum_{j=1}^N p(i,j)$	Sum of rows.
$p_y(i)$	$\sum_{i=1}^N p(i,j)$	Sum of columns.
$\mu_x, \mu_y, \sigma_x, \sigma_y$	–	Mean and standard deviations of p_x and p_y .
N	–	Number of grey levels ($n=256$ for an 8-bit greyscale image)
$p_{x+y}(k)$	$\sum_{i=1}^N \sum_{j=1}^N p(i,j); k = i + j$	Summation across the diagonal of the GLCMs; since GLCMs are symmetric, this operation effectively removes a dimension.
$p_{x-y}(k)$	$\sum_{i=1}^N \sum_{j=1}^N p(i,j); k = i - j $	Summation across the diagonal of the GLCMs; since GLCMs are all symmetric, this operation effectively removes a dimension.
ϵ	–	Arbitrary small positive quantity
HX	$-\sum_{i=1}^N p_x(i) \log \{p_x(i) + \epsilon\}$	Entropy of p_x
HY	$-\sum_{i=1}^N p_y(i) \log \{p_y(i) + \epsilon\}$	Entropy of p_y
HXY	$-\sum_{i=1}^N \sum_{j=1}^N p(i,j) \log \{p(i,j) + \epsilon\}$	Entropy of p (i.e. parameter f_0)
$HXY1$	$-\sum_{i=1}^N \sum_{j=1}^N p(i,j) \log \{p_x(i)p_y(j)\} + \epsilon$	Entropy-based metric
$HXY2$	$-\sum_{i=1}^N \sum_{j=1}^N p_x(i)p_y(j) \log \{p_x(i)p_y(j)\} + \epsilon$	Entropy-based metric

References

- Apostolopoulos, D., Wagner, M., Shamah, B., Pedersen, L., Shillitcut, K., Whittaker, W., 2000. Technology and field demonstration for robotic search for Antarctic meteorites. *Int. J. Robot. Res.* 19 (11), 1015–1032.
- Bajracharya, M., Maimone, M.W., Helmick, D., 2008. Autonomy for Mars rovers: past, present, and future. *Computer* 41, 44–50.
- Cabrol, N., Wettergreen, D., Warren-Rhodes, K., Grin, E., Moersch, J., Diaz, G., Cockell, C., Coppin, P., Demergasson, C., Dohm, J., Ernst, L., Fisher, G., Glasgow, J., Hardgrove, C., Hock, A., Jonak, D., Marinangeli, L., Minkley, E., Ori, G., Smith, T., Stubbs, K., Thomas, G., Wagner, M., Wyatt, M., Boyle, L., 2007. Life in the Atacama: search for life with rovers (science overview). *J. Geophys. Res.* 112, G04S06.
- Castano, R., Estlin, T., Anderson, R.C., Gaines, D.M., Castano, A., Bornstein, B., Chouinard, C., Judd, M., 2007. OASIS: Onboard Autonomous Science Investigation System for opportunistic rover science. *J. Field Robot.* 24 (5), 379–397.
- Ellery, A., Wynn-Williams, D., 2003. Why Raman spectroscopy on Mars? A case of the right tool for the right job. *Astrobiology* 3 (3), 565–579.
- Ellery, A., Wynn-Williams, D., Parnell, J., Edwards, H., Dickensheets, D., 2004. The role of Raman spectroscopy as an astrobiological tool. *J. Raman Spectrosc.* 35, 441–457.
- Erickson, J.K., Adler, M., Crisp, J., Mishkin, A., Welch, R., 2002. Mars exploration rover surface operations. In: 53rd International Astronautics Congress, Houston, TX, Abstract IAC-02-Q.3.1.03.
- Estlin, T., Gaines, D., Chouinard, C., Castano, R., Bornstein, B., Judd, M., Anderson, R. C., 2007. Increased Mars rover autonomy using AI planning, scheduling and execution. In: Proceedings of the IEEE International Conference on Robotics and Automation, Rome, Italy.
- Gallant, M.J., Ellery, A., Marshall, J.A., 2013. Rover-based autonomous science by probabilistic identification and evaluation. *J. Intell. Robot. Syst.* 72 (3–4), 591–613.
- Gallant, M.J., 2011. A Probabilistic Approach to Autonomous Planetary Science with Prime and Scout Rovers. M.A.Sc. Carleton University, Ottawa, Canada, Thesis.
- Gazis, P., Roush, T., 2001. Autonomous identification of carbonates using near-IR reflectance spectra during the February 1999 Marsokhod field tests. *J. Geophys. Res.* 106 (E4), 7765–7773.
- Gor, V., Castano, R., Manduchi, R., Anderson, R.C., Mjolsness, E., 2001. Autonomous Rock Detection for Mars Terrain. American Institute of Aeronautics and Astronautics, Contribution AIAA-01-4597.
- González, R., Woods, R., Eddins, S., 2009. Digital Image Processing Using MATLAB, 2nd Ed Prentice Hall, p. 827.
- Gottlieb, C.C., Kreysig, H.E., 1990. Texture descriptors based on co-occurrence matrices. *Comput. Vis., Graphics, Image Process.* 51, 70–86.
- Griffiths, A., Coates, A., Josset, J.L., Paar, G., Hofmann, B., Pullan, D., Ruffer, P., Sims, M., Pillinger, C., 2005. Beagle 2 stereocamera system. *Planet. Space Sci.* 53, 1466–1482.
- Gulick, V., Morris, R., Ruzon, M., Roush, T., 2001. Autonomous image analyses during the 1999 Marsokhod rover field test. *J. Geophys. Res.* 106 (E4), 7745–7763.
- Halatci, I., Brooks, C.A., Iagnemma, K., 2008. A study of visual and tactile terrain classification and classifier fusion for planetary exploration rovers. *Robotica* 26 (6), 767–779.
- Haralick, R.M., 1979. Statistical and structural approaches to texture. *Proc. IEEE* 67 (5), 786–804.
- Haralick, R.M., Shanmugam, K.S., 1974. Combined spectral and spatial processing of ERTS imagery data. *Remote Sens. Environ.* 3, 3–13.
- Haralick, R.M., Shanmugam, K.S., Dinstein, I., 1973. Textural features for image classification. *IEEE Trans. Syst., Man Cybern.* 6, 610–621.
- Hayes, A., Grotzinger, J.P., Edgar, L.A., Squyres, S.W., Watters, W.A., Sohl-Dickstein, J., 2011. Reconstruction of eolian bed forms and paleo-currents from cross-bedded strata at Victoria Crater, Meridiani Planum, Mars. *J. Geophys. Res.* 116, E00F21.
- Maimone, M., Biesiadecki, J., Tunstel, E., Cheng, Y., Leger, C., 2006. Surface navigation and mobility intelligence on the Mars Exploration Rovers, *Intelligence for Space Robotics*. TSI Press, San Antonio, TX, pp. 45–69, Chapter 3.
- Maki, J., Thiessen, D., Pourangi, A., Kobzeff, P., 2012. The Mars Science Laboratory Engineering Cameras. *Space Science Rev.* Springer Science + Business Media B. V.
- McGuire, P., Gross, C., Wendt, L., Bonnici, A., Souza-Egipsy, V., Ormo, J., Diaz-Martinez, E., Foing, B., Bose, R., Walter, S., Oesker, M., Ontrup, J., Haschke, R., Ritter, H., 2010. Cyborg astrobiologist: testing a novelty detection algorithm on two mobile exploration systems at Rivas Vaciamadrid in Spain and at the Mars Desert Research Station in Utah. *Int. J. Astrobiol.* 9 (1), 11–27.
- McGuire, P., Ormo, J., Martinez, E., Rodriguez, J., Elvira, J., Ritter, H., Oesker, M., Ontrup, J., 2004. Cyborg astrobiologist: first field experience. *Int. J. Astrobiol.* 3 (3), 189–207.
- Milazzo, M.P., Keszthelyi, L.P., Jaeger, W.L., Rosiek, M., Mattson, S., Verba, C., Beyer, R.A., Geissler, P.E., McEwen, A.S., 2009. Discovery of columnar jointing on Mars. *Geology* 37, 171–174.
- Moore, J.M., Howard, A.D., 2005. Large alluvial fans on Mars. *J. Geophys. Res.* 110, E04005.
- Morris, R.V., Ruff, S.W., Gellert, R., Ming, D.W., Arvidson, R.E., Clark, B.C., Golden, D., Siebach, K., Klingelhoefer, G., Schröder, C., Fleischer, I., Yen, A.S., Squyres, S.W., 2010. Identification of carbonate-rich outcrops on Mars by the Spirit Rover. *Sci. Mag.* 329 (5990), 421–424.
- Pedersen, L., 2001. Robotic Rock Classification and Autonomous Exploration. Carnegie Mellon University, Pittsburgh, United States, Ph.D. Thesis.
- Schröder, C., Rodionov, D.S., McCoy, T.J., Jolliff, B.L., Gellert, R., Nittler, L.R., Farrand, W.H., Johnson, J.R., Ruff, S.W., Ashley, J.W., Mittlefehdlt, D.W., Herkenhoff, K.E., Fleischer, I., Haldemann, A.F.C., Klingelhoefer, G., Ming, D.W., Morris, R.V., de Souza Jr, P.A., Squyres, S.W., Weitz, C., Yen, A.S., Zipfel, J., Economou, T., 2008. Meteorites on Mars observed with the Mars exploration rovers. *J. Geophys. Res.* 113, E06S22.
- Sharif, H., 2013. Autonomous Geologist for Planetary Exploration. Carleton University, Ottawa, Canada, M.A.Sc. Thesis.
- Smith, T., Thompson, D., Wettergreen, D., Cabrol, N., Warren-Rhodes, A., Weinstein, S., 2007. Life in the Atacama: science autonomy for improving data quality. *J. Geophys. Res.* 112, G04S03.
- Thompson, D., Nieku, S., Smith, T., Wettergreen, D., 2005. Automatic detection and classification of features of geological interest. In: Proceedings of the IEEE Aerospace Conference, Big Sky, MT.
- Tsaneva, M., 2008. Texture features for segmentation of satellite images. *Cybern. Inf. Technol.* 8 (3), 73–85.
- Van der Sanden, J.J., Hoekman, D.H., 2005. Review of relationship between grey-tone co-occurrence, semivariance, and autocorrelation based image texture analysis. *Can. J. Remote Sens.* 31 (3), 207–213.
- Wagner, M., Apostolopoulos, D., Shillitcut, K., Shamah, B., Simmons, R., Whittaker, W., 2001. Science autonomy system of the Nomad robot. In: Proceedings of the IEEE International Conference on Robotics and Automation, Seoul, Korea.

- Warren-Rhodes, K., Weinstein, S., Piatek, J., Dohm, J., Hock, A., Minkley, E., Pane, D., Ernst, A., Fisher, G., Emani, S., Waggoner, A., Cabrol, N., Wettergreen, D., Grin, E., Coppin, P., Diaz, C., Moersch, J., Oril, G., Smith, T., Stubbs, K., Thomas, G., Wagner, M., Wyatt, M., Boyle, L., 2007. Robotic ecological mapping: habitats and the search for life in the Atacama desert. *J. Geophys. Res.* 112, G04S06.
- Williams, R.M.E., Grotzinger, J.P., Dietrich, W.E., Gupta, S., Sumner, D.Y., Wiens, R.C., Mangold, N., Malin, M.C., Edgett, K.S., Maurice, S., Forni, O., Gasnault, O., Ollila, A., Newsom, H.E., Dromart, G., Palucis, M.C., Yingst, R.A., Anderson, R.B., Herkenhoff, K.E., Le Mouelic, S., Goetz, W., Madsen, M.B., Koefoed, A., Stack, K. M., Rubin, D., Kah, L.C., Bell, J.F.III, Farmer, J.D., Sullivan, R., Van Beek, T., Blaney, D.L., Pariser, O., Deen, R.G., MSL Science Team, 2013. Martian fluvial conglomerates at Gale Crater. *Sci. Mag.* 340 (6136), 1068–1072.
- Woods, M., Shaw, A., Barnes, D., Price, D., Long, D., Pullan, D., 2009. Autonomous science for an ExoMars rover-like mission. *J. Field Robot.* 26 (4), 358–390.